Advances in Water Resources 115 (2018) 185–197

Contents lists available at ScienceDirect

Advances in Water Resources

journal homepage: www.elsevier.com/locate/advwatres

A 1D–2D coupled SPH-SWE model applied to open channel flow simulations in complicated geometries

Kao-Hua Chang[a], Tony Wen-Hann Sheu[a,b,*], Tsang-Jung Chang[c,d]

[a] Department of Engineering Science and Ocean Engineering, National Taiwan University, Taipei 106, Taiwan
[b] Center for Advanced Studies in Theoretical Sciences (CASTS), National Taiwan University, Taipei 106, Taiwan
[c] Department of Bioenvironmental Systems Engineering, National Taiwan University, Taipei 106, Taiwan
[d] Hydrotech Research Institute, National Taiwan University, Taipei 106, Taiwan

ARTICLE INFO

Article history:
Received 13 February 2017
Revised 8 March 2018
Accepted 12 March 2018
Available online 13 March 2018

Keywords:
Smoothed particle hydrodynamics
Shallow water equations
1D–2D coupled
Open channel

ABSTRACT

In this study, a one- and two-dimensional (1D–2D) coupled model is developed to solve the shallow water equations (SWEs). The solutions are obtained using a Lagrangian meshless method called smoothed particle hydrodynamics (SPH) to simulate shallow water flows in converging, diverging and curved channels. A buffer zone is introduced to exchange information between the 1D and 2D SPH-SWE models. Interpolated water discharge values and water surface levels at the internal boundaries are prescribed as the inflow/outflow boundary conditions in the two SPH-SWE models. In addition, instead of using the SPH summation operator, we directly solve the continuity equation by introducing a diffusive term to suppress oscillations in the predicted water depth. The performance of the two approaches in calculating the water depth is comprehensively compared through a case study of a straight channel. Additionally, three benchmark cases involving converging, diverging and curved channels are adopted to demonstrate the ability of the proposed 1D and 2D coupled SPH-SWE model through comparisons with measured data and predicted mesh-based numerical results. The proposed model provides satisfactory accuracy and guaranteed convergence.

1. Introduction

Open channel flow is an essential topic in hydraulics, and studies of this topic range from drainage in artificial channels and rivers (Ying et al., 2004; Burguete et al., 2008) and the design of hydraulic structures such as spillways (Unami et al., 1999) and bridges (Biglari and Sturm, 1998) to flood prevention measures (Hsu et al., 2003). Numerical simulation approaches are extensively used to study open channel flow by solving either 1D or 2D shallow water equations (SWEs) for the discharge, wetted cross-sectional area, flow velocity and depth (Chaudhry, 2008). The SWEs can be derived from the area-integrated and depth-integrated Navier–Stokes equations. In general, 1D SWE models are used to model large open-channel systems because of their high efficiency in comparison with the 2D SWE models. For example, 1D SWE models approximated by the finite difference method (FDM) (Choi and Molinas, 1993), finite element method (FEM) (Sen and Garg, 1998) and finite volume method (FVM) (Sanders et al., 2001) have been successfully applied to model large open-channel flows.

However, the existing 1D SWE models cannot resolve the 2D flow phenomena that can be captured by 2D SWE models, *e.g.*, flows in converging, diverging, or curved channels. Various coupled approaches that combine computationally efficient 1D SWE models with numerically accurate 2D SWE models have been proposed in the past. Effectively exchanging data between the 1D and 2D models is the key to success in these 1D–2D coupled methods. The processes of connecting the 1D and 2D domains in 1D–2D coupled SWE models can be categorized into two types based on the overlapping area (Marin and Monnier, 2009; Fernandez-Nieto et al., 2010; Arico et al., 2016) or the buffer zone (Blade et al., 2012; Morales-Hernandez et al., 2013; Morales-Hernandez et al., 2016). In coupled models of the first type, the 1D model remains intact, and the 2D model is locally employed (so-called local zoom model). Marin and Monnier (2009) first proposed a superposition approach to convert the contribution of the 2D model into the source terms of the 1D governing equations to predict river overtopping flows. In coupled models of the second type, the 1D model is decomposed into the 2D model, and a buffer zone (e.g., control meshes) is established that incorporates the 1D and 2D domains. Blade et al. (2012) proposed a flux-based connection

* Corresponding author at: National Taiwan University, No. 1, Sec. 4, Roosevelt Road, Taipei 10617, Taiwan.
E-mail address: twhsheu@ntu.edu.tw (T.W.-H. Sheu).

https://doi.org/10.1016/j.advwatres.2018.03.009
0309-1708/

that considers the effects of the mass and momentum exchanged between the 1D and 2D domains in natural channels. Morales-Hernandez et al. (2013) developed an approach that accounts for the interactions at the boundaries based on separate mass conservation and mass and momentum conservation strategies in shallow water flow simulations.

Meshless numerical methods, such as the smoothed particle hydrodynamics method (SPH), moving particle semi-implicit method (MPS) and reproducing kernel particle method (RKPM), have attracted increased attention because of their excellent ability to overcome large deformation difficulties that arise from fluid-solid interactions. SPH, the most popular of these methods, is a Lagrangian meshless particle method. SPH was first proposed by Lucy (1977) and Gingold and Monaghan (1977) in their investigations of astrophysical problems. Particles in space move along pathlines in a Lagrangian sense, and SPH has an advantage over mesh-based methods when interfacial flow dynamics in free surface flows Monaghan, 1994), fluid-structure flows (Shao and Gotoh, 2004) and mudflows (Shao and Lo, 2003) are considered. Some significant characteristics of SPH are as follows: (1) unlike the Eulerian conservation equations, there are no nonlinear convective terms in the Lagrangian equations, thereby ensuring that the discretization is Galilean invariant; (2) the interface between two phases can be naturally captured; and (3) the interactions between a fluid and a solid structure can be easily modeled (Bouscasse et al., 2013; Gong et al., 2016). Recently, SPH has also been utilized to solve SWEs (so-called SPH-SWE model) in modeling dam break flows (Wang and Shen, 1999; Rodriguez-Paz and Bonet, 2005; Ata and Soulaimani, 2005; Chang et al., 2011; Kao and Chang, 2012; Xia et al., 2013; Gu et al., 2017), open channel flows (Vacondio et al., 2012; Chang and Chang, 2013; Chen et al., 2015; Chang et al., 2016; Chang et al., 2017) and run-off flows (Chang et al., 2016).

In the SPH literature, Narayanaswamy et al. (2010) addressed the advantage of coupling a 1D finite difference Boussinesq model with 2D SPH Navier–Stokes model in coastal flow simulations. Altomare et al. (2015) presented a hybridization technique to pass information between a 2D wave propagation model and a 3D SPH Navier–Stokes model in real coastal applications. However, no numerical study of coupled SPH-SWE models has been performed. Therefore, we propose a coupled 1D and 2D SPH-SWE model to more efficiently simulate open channel flows with complicated boundaries. In our proposed model, a buffer zone associated with the inflow/outflow boundaries of the 1D and 2D computational domains is defined in the channel interior. This paper focuses on subcritical flows because they are the most common in rivers and open channels. Flows such as those that originate from dam breaking are not easily modeled with this approach. Based on the characteristics of the proposed method, only one variable can be assessed at the inflow/outflow boundaries. In this study, the water discharge and water surface level at the internal boundaries are interpolated to specify the required inflow and outflow boundary conditions, respectively, for the 1D and 2D models.

To the best of our knowledge, all the SPH-SWE models use an SPH summation operator instead of solving the continuity equation to calculate water depth because this approach enhances the numerical stability. In this study, we add the density diffusion term proposed by Molteni and Colagrossi (2009) into the continuity equation for stability enhancement. A comprehensive comparison concerning the accuracy of the water depth and discharge and the computational efficiency of two approaches applied to calculate the variable water depth is performed based on test cases.

This paper is organized as follows. In Section 2, the 1D SWEs for modeling the wetted cross-sectional area and water discharge are presented. Additionally, the 2D SWEs for the water depth and velocity are introduced. Section 3 gives the fundamental SPH operators, and details of how the proposed SPH-SWE model can be implemented are presented. Section 4 is devoted to the treatment of the three boundaries, the wall, inflow/outflow, and internal boundaries, between the 1D and 2D models. Finally, in Section 5 four flow cases are considered in straight, converging, diverging, and curved channels. Each case is solved to verify and validate the proposed model based on the exact solution, the mesh-based numerical results, and measured data.

2. Governing equations

2.1. One-dimensional shallow water equations

The 1D SWEs can be derived from the area-integration of the Navier–Stokes equations (Chaudhry, 2008) and govern the wetted cross-sectional area and water discharge in open channel flows. The Lagrangian form of the 1D SWEs can be written as follows.

$$\frac{DA}{Dt} = -A\frac{\partial u}{\partial x} \tag{1}$$

$$\frac{DQ}{Dt} = -Q\frac{\partial u}{\partial x} - gA\frac{\partial (d_w + z_b)}{\partial x} - gAS_f \tag{2}$$

In the above equations, $\frac{D}{Dt}$ denotes the total derivative term ($\frac{D}{Dt} = \frac{\partial}{\partial t} + \vec{U}\cdot\nabla$). $\vec{U}(u, v)$ is the water velocity vector, where u and v are the x- and y-components of water velocity, respectively. Q denotes the water discharge ($=Au$); A is the wetted cross-sectional area; d_w is the water depth; z_b is the bed elevation; S_f is the friction slope ($=n_{Ma}^2 Q^2/A^2R^{4/3}$); n_{Ma} is the Manning roughness coefficient; R is the hydraulic radius; and g is gravitational acceleration.

2.2. Two-dimensional shallow water equations

By vertically (the direction of water depth) integrating the Navier–Stokes equations, the 2D SWEs for the water depth and velocity derived in (Chaudhry, 2008) can be given in Lagrangian form as follows:

$$\frac{Dd_w}{Dt} = -d_w\nabla\cdot\vec{U} \tag{3}$$

$$\frac{D\vec{U}}{Dt} = -g\nabla(d_w + z_b) - g\vec{S}_f \tag{4}$$

where the friction slope $\vec{S}_f$ used in the 2D model is defined as $n_{Ma}^2|\vec{U}|\vec{U}/d_w^{4/3}$.

3. SPH-SWE model

3.1. SPH operators

Any physical quantity of particle a, such as ϕ_a, can be approximated as follows within the SPH context.

$$\phi\left(\vec{r}_a\right) = \int \phi\left(\vec{r}\right)\omega\left(\vec{r}_a - \vec{r}, h\right)dV \cong \sum_{b=1}^{b=N} m_b\frac{\phi_b}{\rho_b}\omega\left(\left|\vec{r}_{ab}\right|, h_a\right) \tag{5}$$

In the above equation, m_b ($=\rho_b V_b$) is the mass of particle b; ρ_b is the density of particle b, which is defined as $\rho_0 A_b$ in the 1D model and $\rho_0 d_{w,b}$ in the 2D model; ρ_0 is the bulk density of water ($=1000\,\mathrm{kg/m^3}$); V_b is the volume of particle b; $\vec{r}$ is the position vector ($\vec{r} = \vec{r}\,(x)$ in the 1D model and $\vec{r} = \vec{r}\,(x, y)$ in the 2D model); $|\vec{r}_{ab}|$ ($=|\vec{r}_a - \vec{r}_b|$) is the distance between particles a and b; and $\omega(|\vec{r}_{ab}|, h_a)$ is the kernel function of particle a and is denoted as ω_{ab}^a. In this study, the smoothing length of particle a, which is denoted as h_a, is assigned an initial value of $1.4l_0$

($l_0 = \Delta x_0$ in the 1D model and $l_0 = \Delta x_0 = \Delta y_0$ in the 2D model), where Δx_0 and Δy_0 are the initial particle spacings in the x- and y-directions, respectively, and N is the number of particles in the support domain of particle a (Violeau, 2012).

In this study, the SPH gradient operator is expressed in symmetric form and the SPH divergent operator is expressed in asymmetric form Violeau, 2012). These SPH differential operators are shown in Eqs. (6) and ((7):

$$(\nabla\phi)_a = \rho_a \sum_{b=1}^{b=N} m_b \left(\frac{\phi_a}{\rho_a} + \frac{\phi_b}{\rho_b}\right) \nabla_a \omega_{ab}^a \tag{6}$$

$$\left(\nabla \cdot \vec{\phi}\right)_a = -\frac{1}{\rho_a} \sum_{b=1}^{b=N} m_b \left(\vec{\phi}_a - \vec{\phi}_b\right) \cdot \nabla_a \omega_{ab}^a \tag{7}$$

where $\nabla_a \omega_{ab}^a$ denotes $\frac{\partial \omega_{ab}^a}{\partial x_a}\vec{e}_x + \frac{\partial \omega_{ab}^a}{\partial y_a}\vec{e}_y$ and $\vec{e}_x$ and $\vec{e}_y$ are the unit vectors in the directions of the x- and y-axes, respectively.

In addition, the following SPH Laplacian operator is adopted to consider the viscous acceleration proposed by Monaghan (Monaghan, 1992):

$$\left(\nabla \cdot \mu \nabla \vec{U}\right)_a = 2(D_m + 2) \sum_{b=1}^{b=N} V_b \overline{\mu_{ab}} \frac{\vec{U}_{ab} \cdot \vec{r}_{ab}}{\left|\vec{r}_{ab}\right|^2} \nabla_a \omega_{ab}^a \tag{8}$$

where μ is the kinematic viscosity, $\vec{U}_{ab} = \vec{U}_a - \vec{U}_b$ and $\overline{\mu_{ab}} = 0.5(\mu_a + \mu_b)$.

3.2. Discretized shallow water equations

Based on the chosen SPH gradient and the divergent operators shown in Eqs. (6) and (7), the source terms in Eqs. (1) to (4) can be approximated as follows.

$$\left(\frac{DA}{Dt}\right)_a = \sum_{b=1}^{b=N} m_b u_{ab} \overline{\frac{\tilde{\partial}}{\partial x}(\omega_{ab})} \tag{9}$$

$$\begin{aligned}\left(\frac{DQ}{Dt}\right)_a = {} & u_a \sum_{b=1}^{b=N} m_b (u_a - u_b) \overline{\frac{\partial \omega_{ab}}{\partial x}} \\ & - g A_a^2 \sum_{b=1}^{b=N} m_b \left(\frac{\eta_{w,a}}{A_a^2} + \frac{\eta_{w,b}}{A_b^2}\right) \overline{\frac{\partial \omega_{ab}}{\partial x}} - g A_a S_{f,a}\end{aligned} \tag{10}$$

$$\left(\frac{Dd_w}{Dt}\right)_a = \sum_{b=1}^{b=N} m_b \vec{U}_{ab} \cdot \overline{\tilde{\nabla} \omega_{ab}} \tag{11}$$

$$\left(\frac{D\vec{U}}{Dt}\right)_a = -g d_{w,a} \sum_{b=1}^{b=N} m_b \left(\frac{\eta_{w,a}}{d_{w,a}^2} + \frac{\eta_{w,b}}{d_{w,b}^2}\right) \overline{\nabla \omega_{ab}} - g\vec{S}_{f,a} \tag{12}$$

In the above equations, η_w is the water surface level ($= d_w + z_b$), $u_{ab} = u_a - u_b$ and the Wendland function is used as the kernel function (Violeau, 2012).

In our discretized SWEs, the averaged kernel function is considered due to the non-constant smoothing length, *i.e.*, $\overline{\frac{\partial \omega_{ab}}{\partial x}} = 0.5\left(\frac{\partial \omega_{ab}^a}{\partial x_a} + \frac{\partial \omega_{ba}^b}{\partial x_b}\right)$ and $\overline{\nabla \omega_{ab}} = 0.5(\nabla_a \omega_{ab}^a + \nabla_b \omega_{ba}^b)$ Hernquist and Katz, 1989). Given that the mass in the compact domain of a fluid particle is constant, *i.e.*, $\rho h^{D_m} =$ constant, the temporal variation of the smoothing length can be derived as $Dh/Dt = -(h/D_m\rho)D\rho/Dt$, where D_m denotes the number of dimensions in the domain (Altomare et al., 2015). Furthermore, the corrected divergence operator of velocity, *i.e.*, $\tilde{\partial}/\partial x$ in Eq. (9) and $\tilde{\nabla}$ in Eq. (11), as proposed by Bonet and Lok (1999), is used to achieve first-order consistency, as shown in Eqs. (13) and ((14):

$$\frac{\tilde{\partial}\omega_{ab}^a}{\partial x_a} = \frac{\partial \omega_{ab}^a}{\partial x_a} \Big/ \sum_{b=1}^{b=N} V_b x_{ba} \frac{\partial \omega_{ab}^a}{\partial x_a} \tag{13}$$

$$\tilde{\nabla}_a \omega_{ab}^a = L_a^{-1} \nabla_a \omega_{ab}^a \tag{14}$$

$$\text{where } L_a = \begin{bmatrix} \sum_{b=1}^{b=N} V_b x_{ba} \frac{\partial \omega_{ab}^a}{\partial x_a} & \sum_{b=1}^{b=N} V_b y_{ba} \frac{\partial \omega_{ab}^a}{\partial x_a} \\ \sum_{b=1}^{b=N} V_b x_{ba} \frac{\partial \omega_{ab}^a}{\partial y_a} & \sum_{b=1}^{b=N} V_b y_{ba} \frac{\partial \omega_{ab}^a}{\partial y_a} \end{bmatrix},$$

$$x_{ba} = x_b - x_a \text{ and } y_{ba} = y_b - y_a.$$

3.3. Stabilization terms

3.3.1. Artificial viscosity

In the 1D SPH-SWE model, an artificial viscous force proposed by Monaghan (1992,(1994), as expressed in Eq. (15), is applied to prevent the occurrence of a disordered particle distribution.

$$F_a^{\text{art}} = \sum_{b=1}^{b=N} \overline{A_{ab}} \left(V_b \overline{\nu_{ab}^{\text{art}}} \frac{u_{ab} \cdot x_{ab}}{x_{ab}^2 + \varepsilon^2} \overline{\frac{\partial \omega_{ab}}{\partial x}}\right), \tag{15}$$

where $\overline{\nu_{ab}^{\text{art}}} = \alpha \overline{h_{ab}} \overline{c_{ab}}$, $\overline{h_{ab}} = 0.5(h_a + h_b)$, $\overline{c_{ab}} = 0.5(c_a + c_b)$, $\overline{A_{ab}} = 0.5(A_a + A_b)$, $\varepsilon = 10^{-10}$ and α is a parameter employed to control the artificial viscous effect (=0.3 in this study).

3.3.2. Eddy viscosity

As 2D channel flows become turbulent, eddy viscosity effects can no longer be negligibly small, particularly in cases with solid boundaries. Nadaoka and Yagi (1998) noted that the turbulence structure of a shallow water flow can be divided into bed-friction-generated 3D turbulence at length scales less than the water depth and horizontal 2D eddies at much larger length scales. Bed friction plays a key role in transmitting the dissipated energy from horizontal 2D eddies to 3D turbulent processes. Therefore, the LES shallow water model is ideal for describing the development of horizontal, 2D large-scale eddies. Hence, the SPH-LES model proposed by Shao and Gotoh (2004), who introduced an LES model for an SPH solver, is adopted to model the eddy viscosity originating from subparticle-scale eddies that act on fluid particles, as given in Eq. (16).

$$F_a^{eddy} = 4 \sum_{b=1}^{b=N} V_b \frac{\left(d_{w,a}\nu_{t,a} + d_{w,b}\nu_{t,b}\right)}{d_{w,a}} \frac{\vec{U}_{ab} \cdot \vec{r}_{ab}}{\left|\vec{r}_{ab}\right|^2 + \varepsilon^2} \overline{\nabla \omega_{ab}} \tag{16}$$

In the above equation, ν_t is the turbulent kinematic viscosity calculated by $(C_s l_0)^2 \sqrt{2\bar{\bar{S}}:\bar{\bar{S}}}$, where $\bar{\bar{S}}$ is the local strain tensor and C_s is the Smagorinsky constant (=0.5 in this study). A spatial filter with a width determined by $C_s l_0$ is implicitly used in the LES model. As a result, only the solutions of particle-scale variables are obtained.

3.3.3. Density diffusion

Since the continuity equation is independently solved for each fluid particle, oscillatory solutions are frequently found in the density field. Here, based on Molteni and Colagrossi (2009), the density diffusion terms shown in Eqs. (17) and (18) are incorporated into the 1D and 2D SPH-SWE models, respectively, with the aim of suppressing oscillations in the density field.

$$S_a^{1D} = \sum_{b=1}^{b=N} \overline{D_{ab}} V_b (A_a - A_b) \frac{x_{ab}}{x_{ab}^2 + \varepsilon^2} \overline{\frac{\partial \omega_{ab}}{\partial x}} \tag{17}$$

Table 1
Solution algorithms of the modified Verlet scheme employed in the 1D and 2D models.

1D model	2D model
Midpoint step	
$Q_a^{n+1/2} = Q_a^n + 0.5 \cdot \Delta t (\frac{DQ}{Dt})_a^n$	$\vec{U}_a^{n+1/2} = \vec{U}_a^n + 0.5 \cdot \Delta t (\frac{D\vec{U}}{Dt})_a^n$
$A_a^{n+1/2} = A_a^n + 0.5 \cdot \Delta t (\frac{DA}{Dt})_a^n$	$d_{w,a}^{n+1/2} = d_{w,a}^n + 0.5 \cdot \Delta t (\frac{Dd_w}{Dt})_a^n$
$h_a^{n+1/2} = h_a^n[1 - 0.5 \cdot \Delta t \frac{1}{A_a^n} (\frac{DA}{Dt})_a^n]$	$h_a^{n+1/2} = h_a^n[1 - 0.25 \cdot \Delta t \frac{1}{d_{w,a}^n} (\frac{Dd_w}{Dt})_a^n]$
$u_a^{n+1/2} = Q_a^{n+1/2}/A_a^{n+1/2}$	$\vec{r}_a^{n+1/2} = \vec{r}_a^n + 0.5 \cdot \Delta t \cdot \vec{U}_a^n$
$x_a^{n+1/2} = x_a^n + 0.5 \cdot \Delta t \cdot u_a^{n+1/2}$	
Next step	
$Q_a^{n+1} = Q_a^n + \Delta t (\frac{DQ}{Dt})_a^{n+1/2}$	$\vec{U}_a^{n+1} = \vec{U}_a^n + \Delta t (\frac{D\vec{U}}{Dt})_a^{n+1/2}$
$A_a^{n+1} = A_a^n + \Delta t (\frac{DA}{Dt})_a^{n+1/2}$	$\vec{r}_a^{n+1} = \vec{r}_a^{n+1/2} + 0.5 \cdot \Delta t \cdot \vec{U}_a^{n+1}$
$u_a^{n+1} = Q_a^{n+1}/A_a^{n+1}$	$d_{w,a}^{n+1} = d_{w,a}^{n+1/2} + 0.5 \cdot \Delta t (\frac{Dd_w}{Dt})_a^{n+1}$
$x_a^{n+1} = x_a^{n+1/2} + 0.5 \cdot \Delta t \cdot u_a^{n+1}$	$h_a^{n+1} = \frac{h_a^{n+1/2}}{1+0.25 \cdot \Delta t \frac{1}{d_{w,a}^{n+1}} (\frac{Dd_w}{Dt})_a^{n+1}}$
$h_a^{n+1} = \frac{h_a^{n+1/2}}{1+0.5 \cdot \Delta t \frac{1}{A_a^{n+1}} (\frac{DA}{Dt})_a^{n+1}}$	

$$S_a^{2D} = \sum_{b=1}^{b=N} \overline{D_{ab}} V_b \left(d_{w,a} - d_{w,b}\right) \frac{\vec{r}_{ab} \cdot \overline{\nabla \omega_{ab}}}{|\vec{r}_{ab}|^2 + \varepsilon^2} \tag{18}$$

where $\overline{D_{ab}} = \beta \overline{h_{ab}} \overline{c_{ab}}$ and $\beta = 0.2$ in this study.

3.4. Time integration method

A modified Verlet scheme proposed by Molteni and Colagrossi (2009) is adopted in this study. This approach enables the use of large Courant–Friedrichs–Lewy (CFL) numbers in the process of updating the solutions at the next time step. Table 1 shows the algorithms of the modified Verlet scheme for the 1D and 2D models. The time step (Δt) that satisfies the CFL stability condition is as follows:

$$\Delta t \leq CFL \cdot \min_a \left(\frac{l_0}{|\vec{U}_a| + c_a} \right). \tag{19}$$

In this study, we set *CFL* to 0.8.

4. Boundary treatment

4.1. Wall boundary

In the 2D model, the ghost particle technique developed by Colagrossi and Landrini (2003) is adopted to specify the wall boundary condition. In this study, four layers of ghost particles are involved in the computations of the water depth, pressure force and viscous force of each fluid particle, as schematically shown in Fig. 1. These ghost particles are associated the velocity-divergence operator, the gradient operator of water depth, and the velocity-Laplacian operator. For the ghost particles influenced by the velocity-divergence operator, both the normal and tangent components of their velocities are equal to zero due to the stationary non-slip walls (Bouscasse et al., 2013).

To estimate the viscous interaction between the fluid and ghost particles, mirror points, such as point *c* in Fig. 1, are generated using a mirroring technique along the plane of symmetry. Following the work of Bouscasse et al. (2013), in the presence of free-slip boundary conditions, the normal and tangential components of the velocity of each ghost particle are identical to those at its mirror point. However, in the case of non-slip boundary conditions, the tangential velocity of each ghost particle is specified with the opposing sign as that at the mirror point, and the normal velocity of each ghost particle remains the same as that at the mirror point.

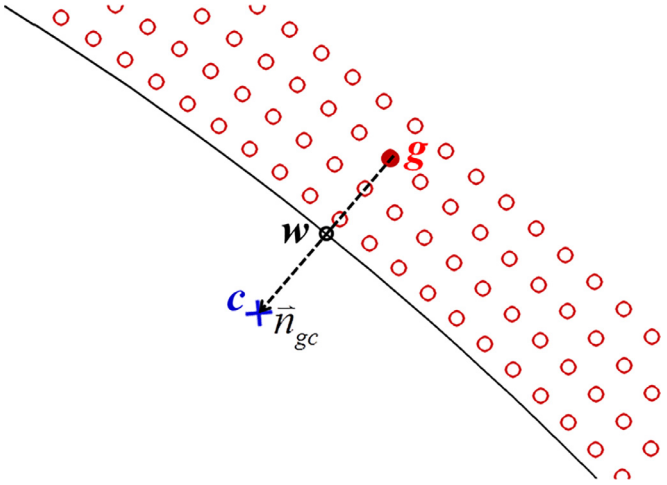

Fig. 1. The schematic of the wall boundary treatment.

To calculate the gradient operator of water depth for ghost particles, the impermeable boundary condition shown in Eq. (20) is applied (Bouscasse et al., 2013).

$$\left(\frac{D\vec{u}}{Dt}\right)_w \cdot \vec{n} = \left[-g\nabla(d_w + z_b) - g\vec{S}_f\right]_w \cdot \vec{n} = 0 \tag{20}$$

Rearranging Eq. (20) leads to the following formula.

$$\left(\frac{\partial d_w}{\partial n}\right)_w = -\left(\nabla z_b + \vec{S}_f\right)_w \cdot \vec{n} \tag{21}$$

Taking the water depth, bed elevation, and water velocity at mirror point *c* into consideration, the water depth of ghost particle *g* can be determined as follows.

$$d_{w,g} = \sum_{b=1, b\in f}^{b=N} V_b \left[d_{w,b} - l_{gc} \left(\nabla z_{b,b} - \vec{S}_{f,b} \right) \cdot \vec{n}_{gc} \right] \tilde{\omega}_{cb}^c \tag{22}$$

In the above equation, $\vec{n}_{gc}$ denotes the unit normal vector ($= (\vec{r}_c - \vec{r}_g)/|\vec{r}_c - \vec{r}_g|$), $l_{gc} = |\vec{r}_c - \vec{r}_g|$. Additionally, $\tilde{\omega}_{cb}^c$ is the corrected kernel function, which can be represented as follows (Randles and Libersky, 1996):

$$\tilde{\omega}_{cb}^c = \frac{\omega_{cb}^c}{\sum_{b=1, b\in f}^{b=N} V_b \omega_{cb}^c} \tag{23}$$

where $h_c = 1.4 l_0$.

4.2. Inflow/outflow boundary

In this study, three types of fluid particles, namely, inflow particles (rectangular points), inner particles (circle points) and outflow particles (triangular points), are used to resolve the problems related to the inflow/outflow boundaries, as schematically shown in Fig. 2. Since SPH is an explicit method, the inflow/outflow boundary conditions must be determined prior to solving the governing equations at each time step. Therefore, we adopt the specified time interval method (Chaudhry, 2008) to calculate unknown variables at the inflow/outflow boundaries. Fig. 2(a) depicts the directions of the characteristic lines. In the presence of a subcritical flow at the inflow boundary, the water discharge is prescribed, and the water depth is obtained by solving Eq. (24) along the negative characteristic line *LP* schematically shown in Fig. 2(a) via Newton–Raphson iterations.

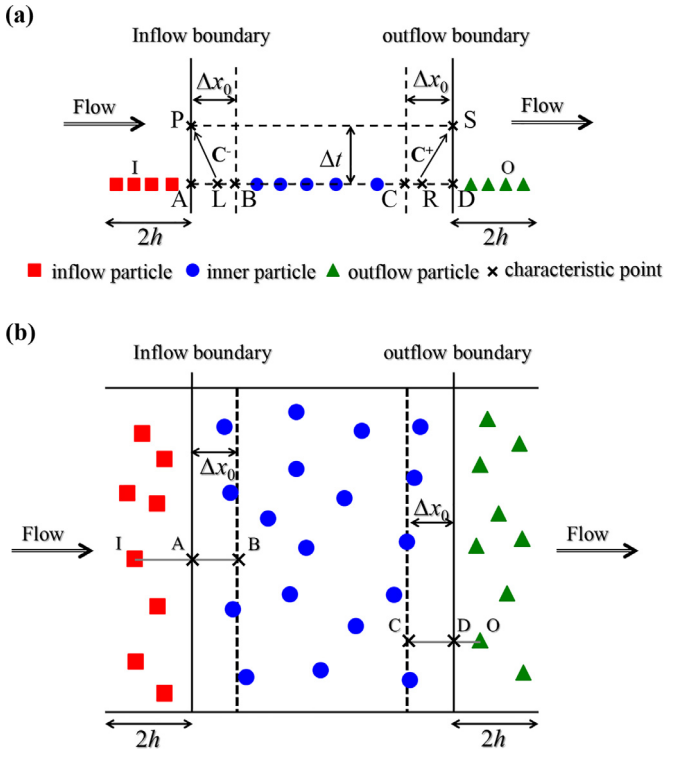

Fig. 2. The schematic of the inflow/outflow boundaries in (a) 1D and (b) 2D.

$$Q_p = A_P u_P = A_P \left[u_L + \frac{g}{c_L}(d_{w,P} - d_{w,L}) - g\left(\left(\frac{\partial z_b}{\partial x} \right)_L + S_{f,L} \right) \Delta t \right] \tag{24}$$

For a subcritical flow specified at the outflow boundary, the water depth is prescribed, and the water discharge is determined from Eq. (25) along the positive characteristic line *RS* shown in Fig. 2(a).

$$Q_S = A_S u_S = A_S \left[u_R - \frac{g}{c_R}(d_{w,S} - d_{w,R}) - g\left(\left(\frac{\partial z_b}{\partial x} \right)_R + S_{f,R} \right) \Delta t \right] \tag{25}$$

One can refer to (Vacondio et al., 2012; Chang and Chang, 2013; Federico et al., 2012) for additional details of this method.

In the treatment of 2D inflow/outflow boundary conditions, the 1D specified time interval method is applied. In this case, no characteristic lines are used. When a subcritical flow occurs at the inflow boundary, the projection point A of particle I on the inflow boundary, as shown in Fig. 2b, is identified. Then, the water depth at point A obtained by solving Eq. (24) is specified as the water depth of inflow particle I. Similarly, if a subcritical flow is considered at the outflow boundary, the water discharge of outflow particle O is equal to the water discharge at projection point D on the outflow boundary obtained using Eq. (25), as shown in Fig. 2(b).

In addition, virtual bed particles are introduced to describe the bed elevation and the roughness (Vacondio et al., 2012). The volume of each virtual bed particle equals l_0, and the bed elevation and the roughness of each fluid particle a are computed from Eq. (26).

$$z_{b,a} = \sum_{b=1, b\in vb}^{b=N} V_b z_{b,b} \tilde{\omega}_{ab}^b, \; n_{Ma,a} = \sum_{b=1, b\in vb}^{b=N} V_b n_{Ma,b} \tilde{\omega}_{ab}^b \tag{26}$$

In the above equation, the subscript *vb* denotes the virtual bed particle and $h_{b\in vb} = 1.4 l_0$.

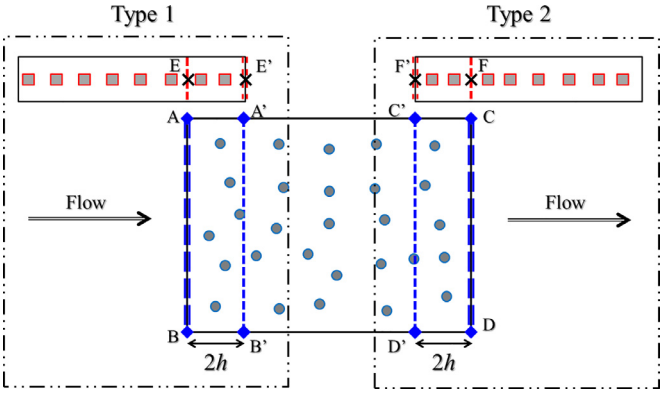

Fig. 3. The schematic of the internal boundaries.

4.3. Internal boundary between the 1D and 2D models

In the proposed coupled model, we use the concept introduced by Narayanaswamy et al. (2010) to choose a buffer zone that connects the 1D domain and the 2D domain. There are two types of connections. The first type includes a 1D model at the upstream side and a 2D model at the downstream side, and the second includes a 2D model at the upstream side and a 1D model at the downstream side, as shown in Fig. 3. For the first type of connection, the locations of section E and section A'B' in the buffer zone are the same as the inflow boundary of the 2D model and the outflow boundary of the 1D model. Similarly, for the second type of connection, the locations of section CD and section F in the buffer zone are the same as the inflow boundary of the 1D model and the outflow boundary of the 2D model. Here, we call the inflow/outflow boundaries of the buffer zone the internal boundaries.

By exchanging the dependent variables in the 1D and 2D models at the internal boundaries, one can obtain the required inflow/outflow boundary conditions and perform computations at the next time step. As subcritical flows form at the internal boundaries, the model at the upstream side provides the inflow boundary condition of water discharge for the model at the downstream side, *i.e.*, $Q_{\overline{AB}} = Q_E$ for the first connection and $Q_{F'} = Q_{\overline{C'D'}}$ for the second connection, where $Q_E = \sum_{b=1, b\in fl, a\in E}^{b=N} V_b Q_b \tilde{\omega}_{ab}^a$ and $Q_{\overline{C'D'}} = \int_{l=\overline{C'D'}} (\sum_{b=1, b\in fl, a\in\overline{C'D'}}^{b=N} V_b (\vec{U}_b \cdot \vec{n}_{\overline{C'D'}}) \tilde{\omega}_{ab}^a) dl$. Similarly, the model at the downstream side provides the outflow boundary condition of the water surface level for the model at the upstream side, *i.e.*, $\eta_{w,E'} = \eta_{w,\overline{A'B'}}$ for the first connection and $\eta_{w,\overline{CD}} = \eta_{w,F}$ for the second connection, where $\eta_{w,\overline{A'B'}} = \frac{1}{l} \int_{l=\overline{A'B'}} (\sum_{b=1, b\in fl, a\in\overline{A'B'}}^{b=N} V_b \eta_{w,b} \tilde{\omega}_{ab}^a) dl$ and $\eta_{w,F} = \sum_{b=1, b\in fl, a\in F}^{b=N} V_b \eta_{w,b} \tilde{\omega}_{ab}^a$. In the above equations, the subscript *fl* stands for fluid particles, and the smoothing length of interpolation point a is $1.4 l_0$ in all interpolations. Thus, we can obtain one boundary condition at the inflow/outflow boundaries of the 1D and 2D models and solve the characteristic equations shown in Section 4.2 to determine another required inflow/outflow boundary condition. In the current study, the width of the buffer zone is chosen as $2h$, where h is equal to $2l_0$. This value ensures that the SPH summation includes the complete support domain at the boundaries of the buffer zone. Moreover, the convergence of the boundary conditions in the buffer zone will be guaranteed. As the initial particle spacing approaches zero, the buffer zone will shrink to a point. Thus, all boundary conditions at the internal boundary are identical for the 1D and 2D models.

Table 2a
Non-dimensional L_2 norms and convergence rates of water depth and velocity for the summation approach in calculating the water depth.

Initial particle spacing (l_0) (m)	$L_2(d_w)$	$L_2(u)$	$L_2(v)$
80	2.73E−04	6.05E−04	3.78E−04
40	1.94E−04	2.09E−04	1.95E−04
20	1.19E−04	1.76E−04	1.16E−04
Convergence rate	0.60	0.89	0.85

Table 2b
Non-dimensional L_2 norms and convergence rates of water depth and velocity for the continuity approach in calculating the water depth.

Initial particle spacing (l_0) (m)	$L_2(d_w)$	$L_2(u)$	$L_2(v)$
80	1.21E−04	5.86E−04	3.71E−04
40	4.49E−05	1.62E−04	1.68E−04
20	3.20E−05	9.39E−05	8.68E−05
Convergence rate	0.96	1.32	1.05

5. Validation

In this section, a straight channel is chosen in our simulation to assess the performance of the two approaches to calculate the water depth. The first approach uses the SPH summation operator.

$$d_{w,a} = \sum_{b=1}^{b=N} m_b \omega\left(\left|\vec{r}_{ab}\right|, h_a\right) \tag{27}$$

Since the non-constant smoothing length is calculated by $h_a = h_{0,a}(\frac{d_{w0,a}}{d_{w,a}})^{1/2}$, where d_{w0} and h_0 are the water depth and smoothing length at the beginning of the simulation, respectively, Eq. (27) becomes nonlinear. A Newton–Raphson iteration is applied to solve Eq. (25) (Rodriguez-Paz and Bonet, 2005; Vacondio et al., 2012). The second approach algebraically solves the SPH-discretized continuity equation given in Eq. (11). Hereafter, we call the first and second approaches the summation and continuity approaches, respectively.

Next, three cases involving converging, diverging and curved channels are investigated to assess the performance of the proposed 1D and 2D coupled SPH-SWE model. All the channels are rectangular, horizontal and frictional. Numerical simulations were performed on an Intel (R) Core (TM) i7-2600 CPU 3.4 GHz PC equipped with 4GB of RAM. In addition, a non-dimensional L_2 norm for any physical quantity (ϕ) is applied to calculate the convergence rate.

$$L_2(\phi) = \sqrt{\frac{1}{N}\sum_{i=1}^{N}\left(\frac{\phi^{SPH} - \phi^{EXT}}{\phi^{EXT}}\right)^2} \tag{28}$$

In the above equation, N is the number of particles at fixed points in the domain and the superscripts SPH and EXT denote the numerical and exact solutions, respectively.

5.1. Straight channel flow simulation

The first simulation involves a straight channel of length 1000 m and width 400 m. This channel was considered by Vacondio et al. (2012) in their simulation using an SPH summation operator to calculate the water depth. The Manning roughness coefficient is 0.0308 s/m$^{1/3}$. The exact solutions of the unit water discharge (15 m^2/s) and water depth (5 m) are prescribed at the inflow and outflow boundaries, respectively.

Three different initial particle spacings of 80 m, 40 m, and 20 m are used to analyze the accuracy and convergence. The non-dimensional L_2 norms based on the water depth and the velocity are calculated as follows.

$$L_2(d_w) = \sqrt{\frac{1}{N}\sum_{i=1}^{N}\left(\frac{d_{w,i}^{SPH} - d_w^{EXT}}{d_w^{EXT}}\right)^2},$$
$$L_2(u) = \sqrt{\frac{1}{N}\sum_{i=1}^{N}\left(\frac{u_i^{SPH} - u^{EXT}}{\sqrt{g d_w^{EXT}}}\right)^2},$$
$$L_2(v) = \sqrt{\frac{1}{N}\sum_{i=1}^{N}\left(\frac{v_i^{SPH} - v^{EXT}}{\sqrt{g d_w^{EXT}}}\right)^2} \tag{29}$$

In the above, d_w is the water depth ($d_w^{EXT} = 5$ m), u is the x-component velocity ($u^{EXT} = 3$ m/s), v is the y-component velocity ($v^{EXT} = 0$ m/s), and N is the number of particles in the domain. The accuracy and the convergence of the two approaches to calculate the water depth are given in Tables 2a and 2b. The continuity approach is more accurate than the summation approach in calculating the velocity and the water depth. Fig. 4 presents the simulated water discharge profiles of the two approaches for the case of an initial particle spacing of 20 m. As shown in Fig. 4, the continuity approach exhibits better mass conservation than the summation approach. $L_2(Q)$ of the summation approach is 1.02E−04, and $L_2(Q)$ of the continuity approach is 3.81E−05. In addition, the continuity approach achieves a faster convergence speed. The convergence rates based on the water depth and the velocity approach unity. For the summation approach, the water depth errors mainly occur in the vicinity of the wall boundaries and are not rapidly reduced by decreasing the initial particle spacing. This issue is reflected by the low convergence rates in Table 2a.

Table 3 lists the CPU times for each approach involving 1159 particles, and the total simulation time is 6000 s. The summation approach takes 1.1 times the CPU time consumed by the continuity

Table 3
The CPU times for all the study cases.

	Total simulation time (sec)	Summation Initial particle number CPU time (sec)	Continuity Initial particle number CPU time (sec)	Speed-up ratio
Case 1	6000	1159 1.05E+03	1159 9.66E+02	1.1
	Total simulation time (sec)	2D SPH-SWE model Initial particle number CPU time (sec)	1D–2D SPH-SWE model Initial particle number CPU time (sec)	Speed-up ratio
Case 2	200	27679 6.00E+04	13672 2.83E+04	2.1
Case 3	200	27359 6.02E+04	12602 3.09E+04	2.0
Case 4	200	23354 2.36E+04	10923 1.10E+04	2.1

Table 4
The locations of the inflow/outflow boundaries in the 1D domain in the 1D–2D coupled SPH-SWE model.

	Channel 1		Channel 2		Channel 3	
	Inflow boundary	Outflow boundary	Inflow boundary	Outflow boundary	Inflow boundary	Outflow boundary
Case 2	$x = 5B$	$x = B - 4l_0$	$y = -4B$	$y = -B + 4l_0$	$x = -6B + 4l_0$	$x = -8B$
Case 3	$x = -10B$	$x = -2B + 4l_0$	$x = 4B - 4l_0$	$x = 10B$	$y = 7B - 4l_0$	$y = 10B$
Case 4	$x = -7B$	$x = -B + 4l_0$	$x = -2B + 4l_0$	$x = -4B$	–	–

B is the channel width, and l_0 is the initial particle spacing.

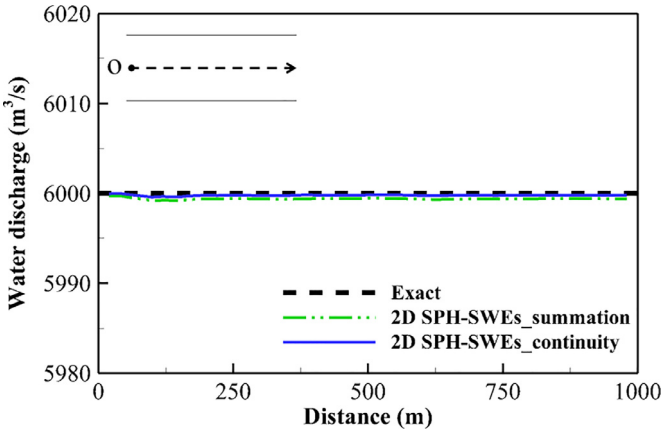

Fig. 4. The simulated water discharge profiles of the two approaches in calculating the water depth in the straight channel.

approach. We believe that the approach of calculating water depth via solving the continuity equations can efficiently yield a higher accuracy than the summation approach for the water depth and yields a higher degree of mass conservation. Therefore, in the following case studies, only the continuity approach is used in the two SPH-SWE models.

5.2. Converging channel flow simulation

A converging channel with a junction angle of 90° was experimentally studied by Weber et al. (2001) and is adopted in this study for comparison. The converging channels in the 2D and 1D–2D coupled models are schematically shown in Fig. 5(a) and (b), where the solid lines denote the 2D domain and the dash lines denote the 1D domain. Table 4 shows the locations of the inflow/outflow boundaries in the 1D domain. The channel width is 0.914 m, and the Manning's roughness coefficient of 0.011 s/m$^{1/3}$ accounts for bed friction. A water discharge of 0.043 m^3/s and water depth ($d_{w,0}$) of 0.296 m are prescribed as the inflow and outflow boundary conditions in the main channel, respectively, and a water discharge of 0.127 m^3/s is prescribed as the inflow boundary condition in the branch channel. The outflow discharge in the main channel is therefore equal to 0.17 m^3/s. The initial particle spacing is set to 0.02285 m in the 1D and 2D models, and the maximum time step is 0.007 s.

The depth contours and the streamline configurations for the two SPH-SWE models are plotted in Fig. 6. The water depths gradually decrease downstream of the channel convergence section, and the flow convergence results in the formation of a vortex. Fig. 7 shows the simulated profiles of water depths at three lateral distances along the main channel. The results obtained by the investigated SPH-SWE models are all consistent with the measured data presented by Weber et al. (2001) and the FEM-based simulation results of Song et al. (2012). A comparison of the simulated profiles of water discharge along the main channel based on the two SPH-SWE models is presented in Fig. 8. When the flow from

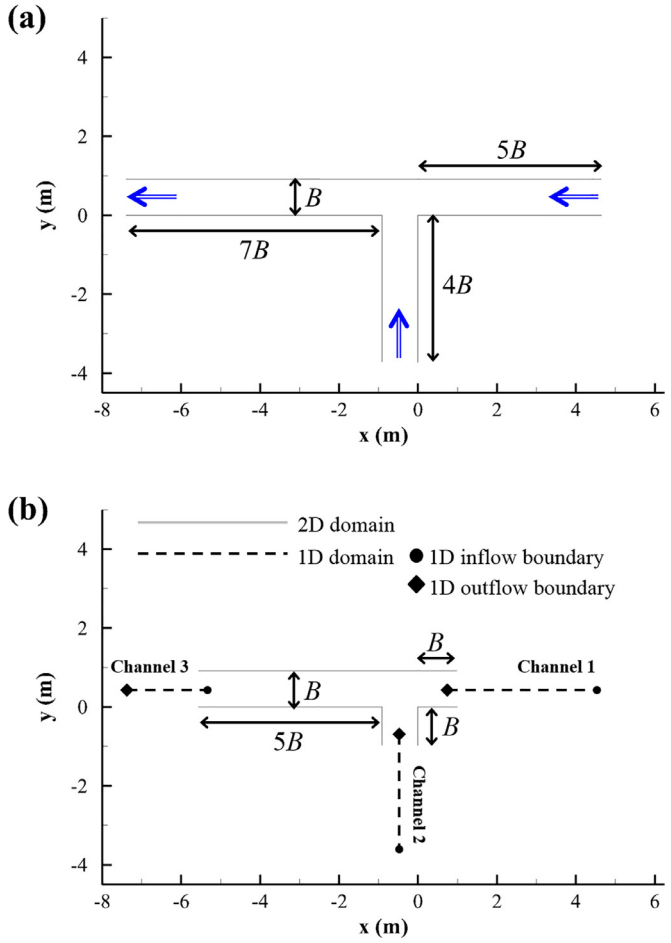

Fig. 5. The schematic of the converging channel: (a) 2D model and (b) 1D–2D coupled model.

Table 5
The convergence rates in 1D and 2D domains in the 1D–2D coupled model.

	Involved initial particle spacing (l_0) (m)	Convergence rate	
		1D	2D
Case 2	$l_0 = 0.0914, 0.0457, 0.02285$	0.99	0.88
Case 3	$l_0 = 0.03, 0.015, 0.0075$	1.40	1.49
Case 4	$l_0 = 0.08, 0.04, 0.02$	1.07	1.15

the upstream side of the main channel converges at the junction with the flow from the branch channel, the discharge increases to 0.17 m^3/s. In the 1D–2D coupled model, $L_2(Q)$ in the 1D domain is 1.05E−02, and $L_2(Q)$ in the 2D domain is 7.58E−03. As listed in Table 5, the convergence rates based on the water discharge in the 1D and 2D domains are 0.99 and 0.88, respectively. In addition, Table 3 shows that the 2D model takes 2.1 times the CPU time required by the 1D–2D coupled model. Both the 1D–2D cou-

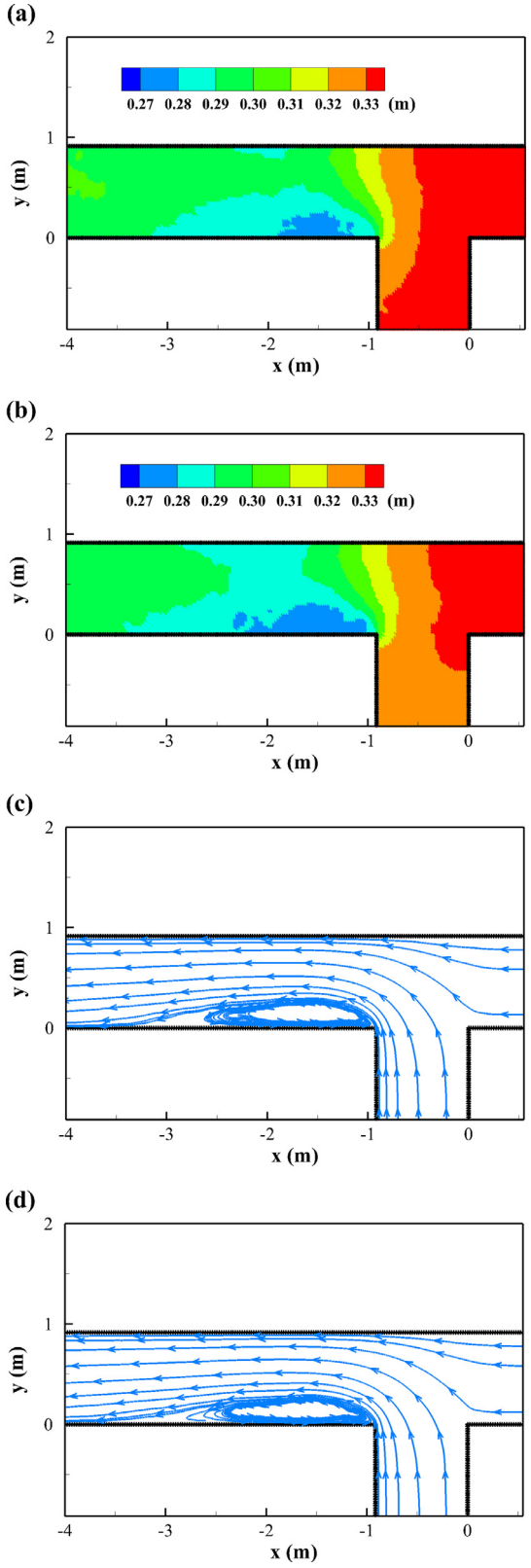

Fig. 6. The water depth contours simulated by the (a) 2D model and (b) 1D–2D coupled model. The streamlines simulated by the (c) 2D model and (d) 1D–2D coupled model in the converging channel.

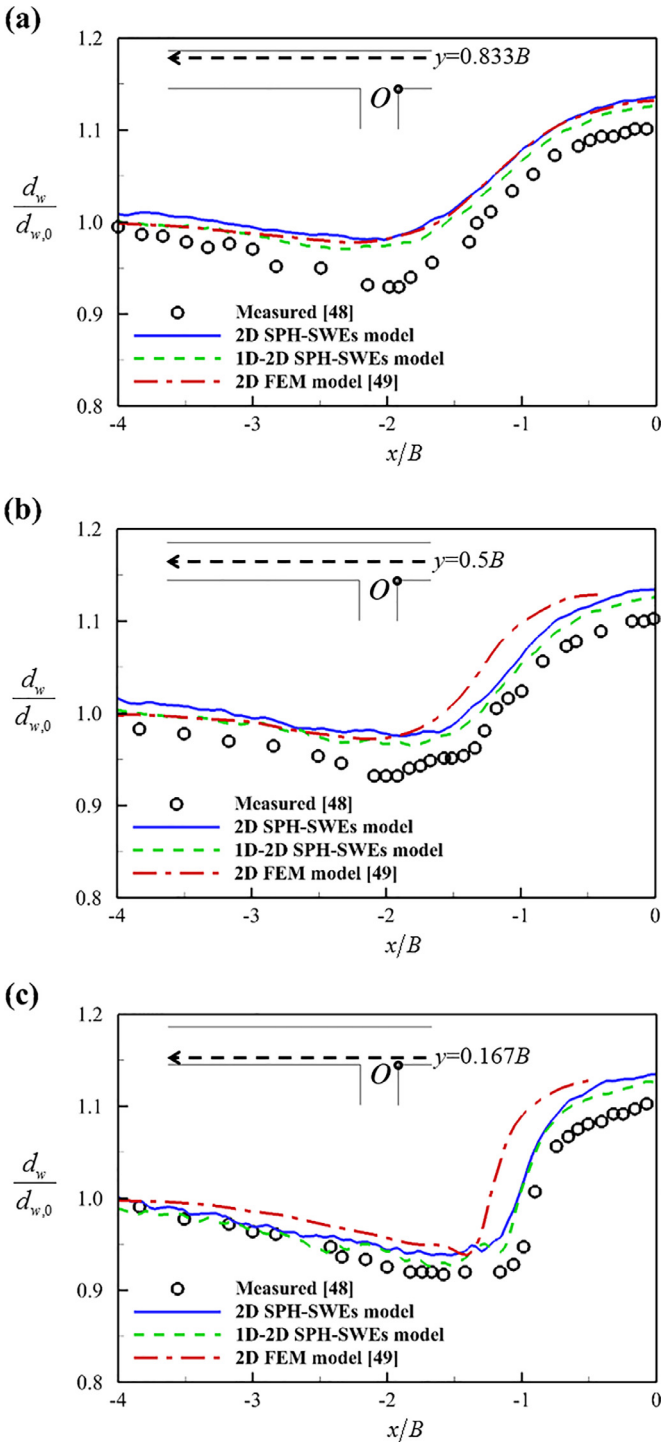

Fig. 7. The simulated water depth profiles in the converging channel: (a) $y = 0.833B$, (b) $y = 0.5B$ and (c) $y = 0.167B$.

pled model and 2D model results can be efficiently obtained for the converging channel.

5.3. Diverging channel flow simulation

In the third simulation case, a diverging channel with a junction angle of 90° that was experimentally studied by Shettar and Murthy (1996) is investigated. This channel has a width of 0.3 m, and the channel bottom is rough, with a Manning's roughness coefficient of 0.011 s/m$^{1/3}$. Fig. 9 shows the schematic of the diverg-

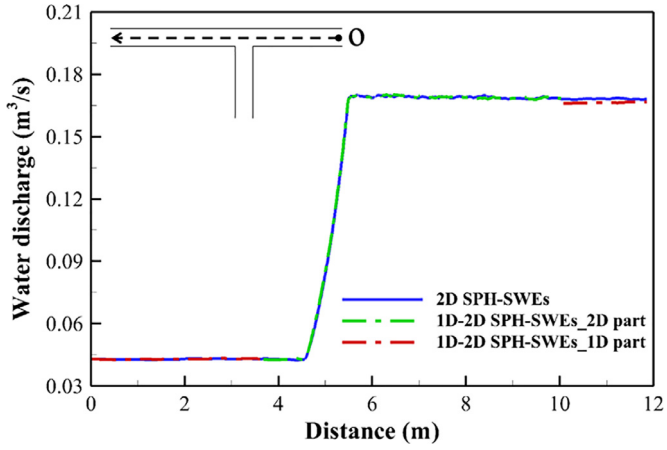

Fig. 8. The simulated profiles of water discharge in the converging channel.

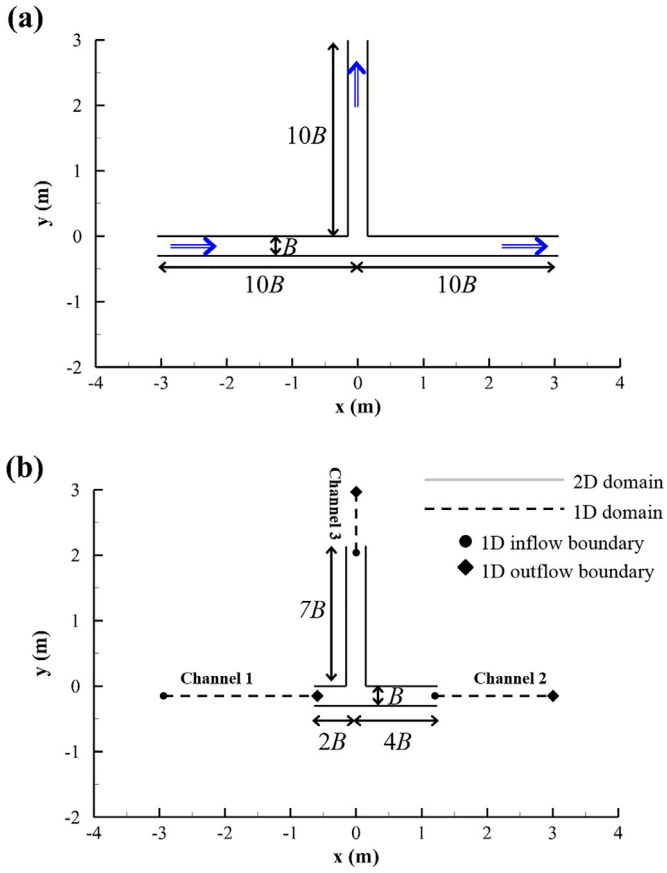

Fig. 9. The schematic of the diverging channel: (a) 2D model and (b) 1D–2D coupled model.

ing channel investigated using the 2D and 1D–2D coupled models. The locations of the inflow/outflow boundaries in the 1D domain are given in Table 4. As boundary conditions, a water discharge of 0.005673 m^3/s and water depth of 0.0541 m are prescribed at the inflow and outflow boundaries of the main channel, respectively, and a water depth of 0.0458 m is specified at the outflow boundary of the branch channel. The initial particle spacing is 0.01 m in both the 1D and 2D models, and the maximum time step is 0.007 s.

The depth and streamline contours are plotted in Fig. 10, which shows that the water depth at the downstream side of the main channel increases and a vortex forms at the left side of the inlet in the branch channel as the flow separates at the diverging junction.

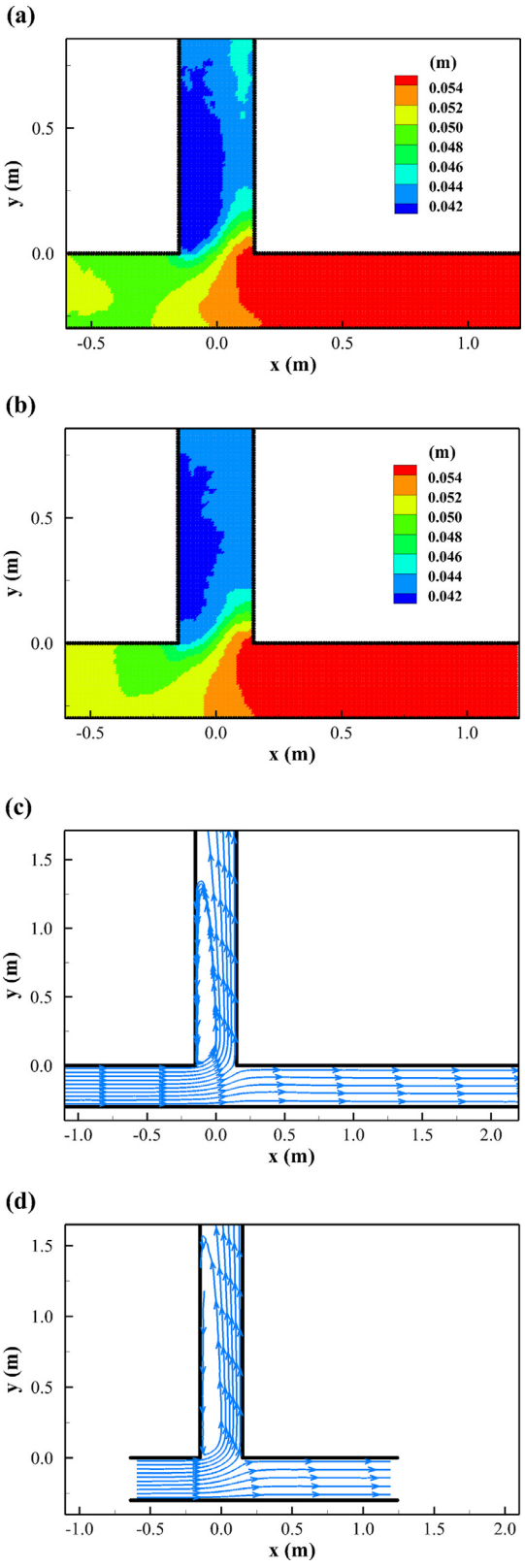

Fig. 10. The water depth contours simulated by the (a) 2D model and (b) 1D–2D coupled model. The streamlines simulated by the (c) 2D model and (d) 1D–2D coupled model in the diverging channel.

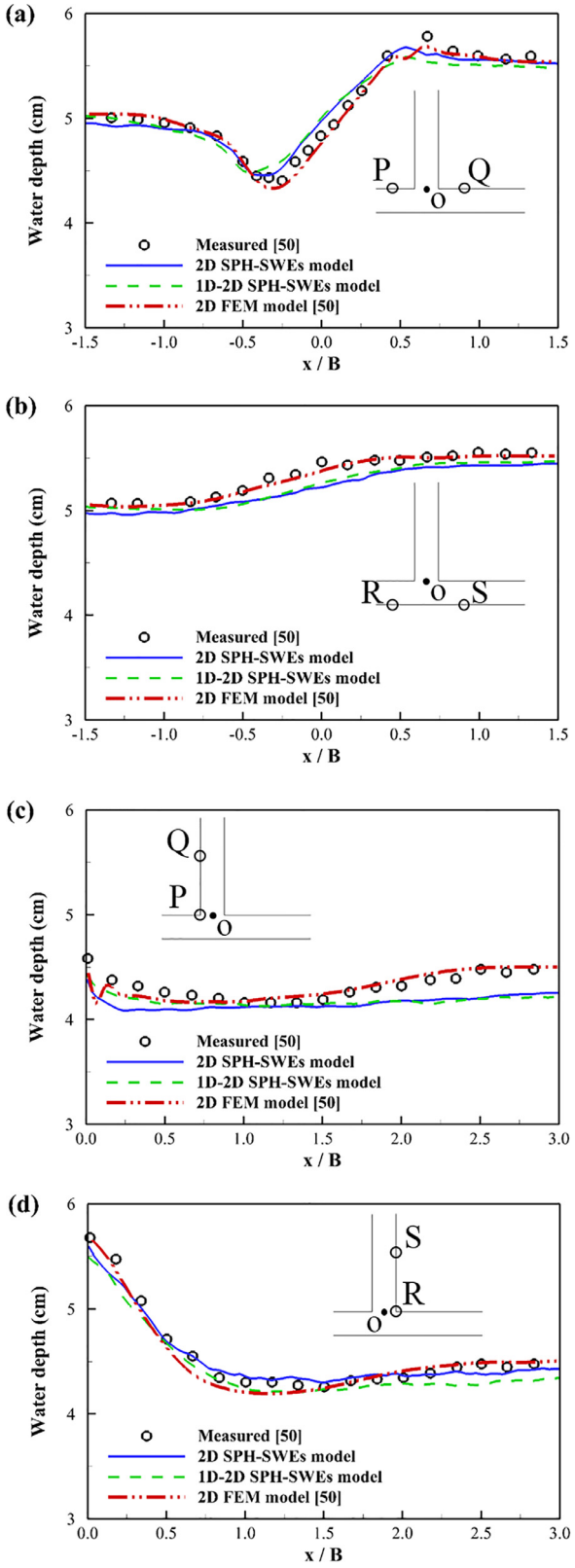

Fig. 11. The simulated profiles of water depth in the diverging channel: (a) along PQ; (b) along RS in the main channel; (c) along PQ; and (d) along RS in the branch channel.

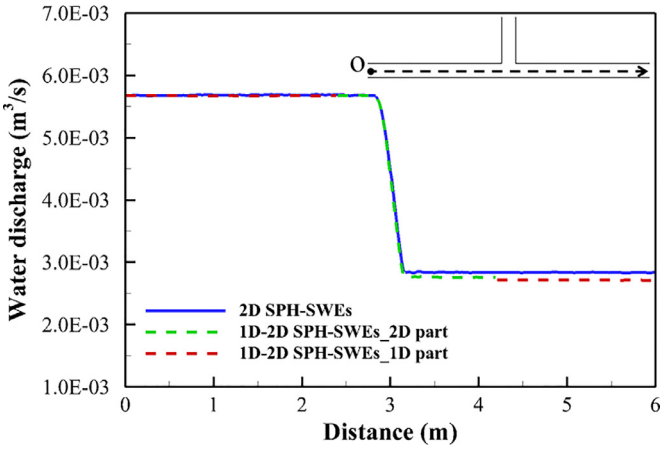

Fig. 12. The simulated profiles of water discharge in the diverging channel.

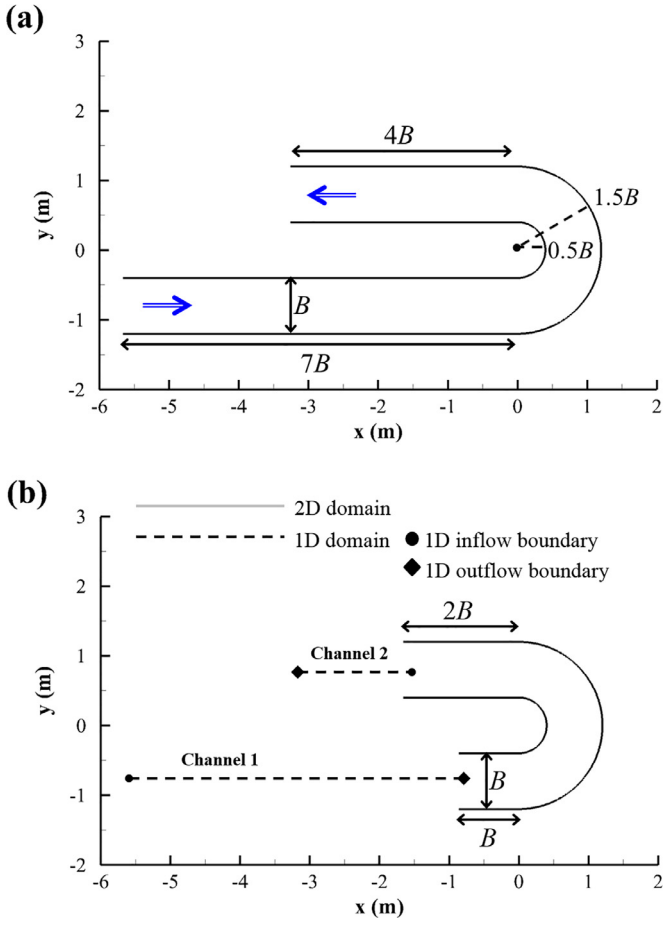

Fig. 13. The schematic of the curved channel: (a) 2D model and (b) 1D–2D coupled model.

As shown in Fig. 11, the simulated water depths were compared with the data collected by Shettar and Murthy (1996). The variations in water depth along the four walls predicted using the two proposed SPH-SWE models exhibit good agreement with the measured data. However, the SPH-based simulation results are less accurate than those predicted by the FEM-based method because the SPH-based solutions at the walls are obtained based on an extrapolation from the inner fluid particles. Fig. 12 displays the SPH-based simulated profiles of water discharge along the main channel in the two SPH-SWE models. Notably, the accuracy and convergence

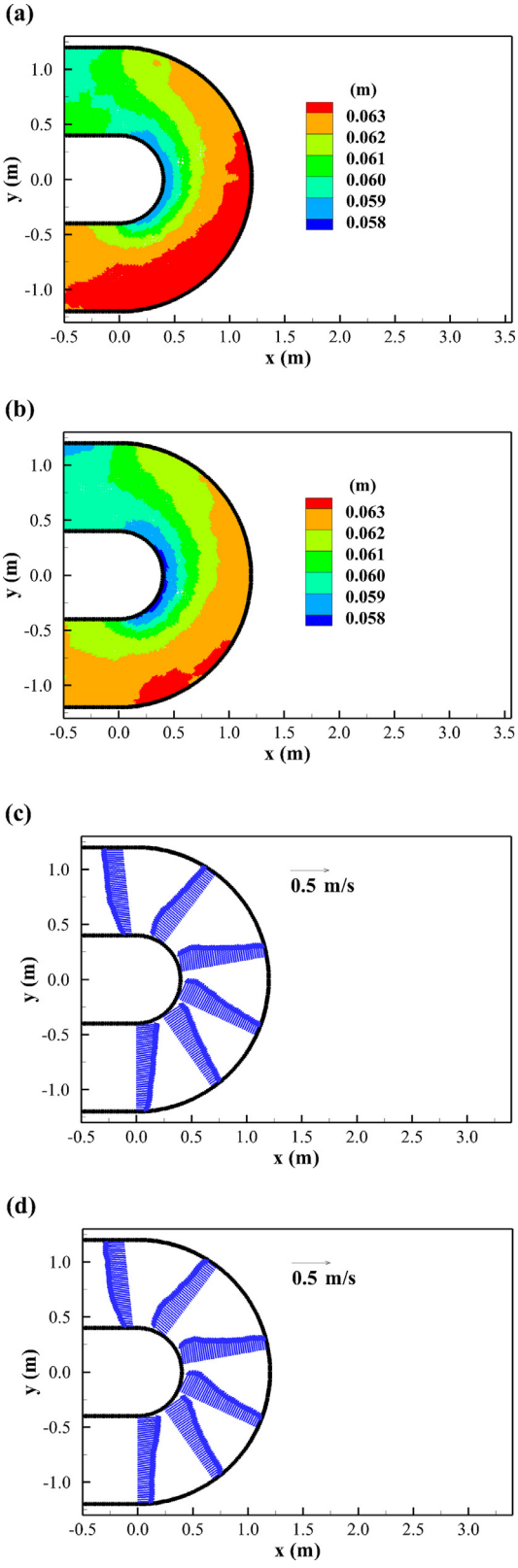

Fig. 14. The water depth contours simulated by the (a) 2D model and (b) 1D–2D coupled model. The profiles of velocity vectors simulated by the (c) 2D model and (d) 1D–2D coupled model in the curved channel.

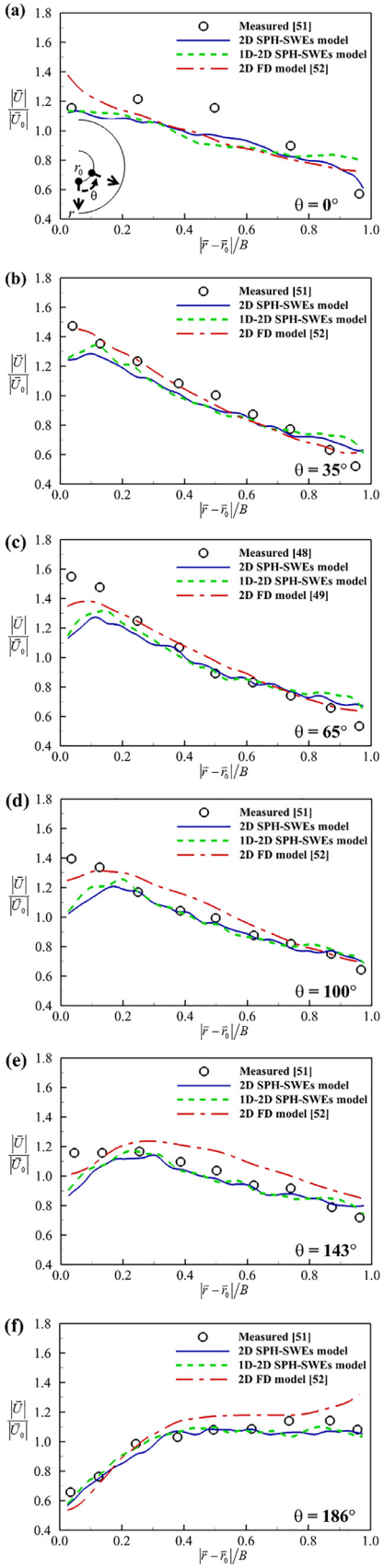

Fig. 15. The simulated profiles of water velocity in the curved channel: (a) $\theta = 0°$, (b) $\theta = 35°$, (c) $\theta = 65°$, (d) $\theta = 100°$, (e) $\theta = 143°$ and (d) $\theta = 186°$

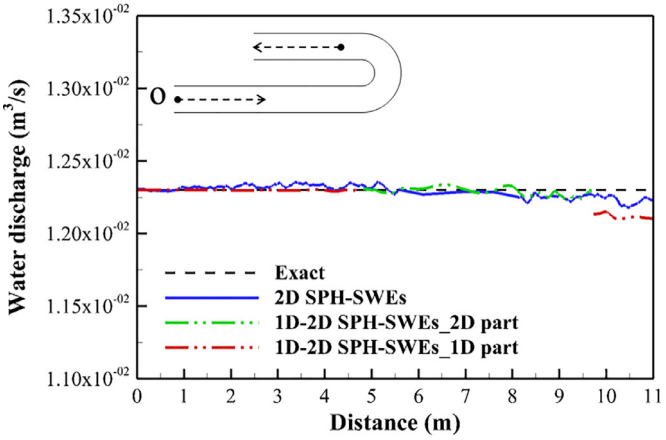

Figure 16. The simulated profiles of water discharge in the curved channel.

of the 1D–2D coupled model were investigated. $L_2(Q)$ in the 1D domain is 1.34E−02, and $L_2(Q)$ in the 2D domain is 2.86E−03. The convergence rates based on water discharges of 1.40 and 1.49 in the 1D and 2D domains, respectively, are shown in Table 5. Additionally, the CPU times are shown in Table 3. The ratio of the CPU time of the 2D model to that of the 1D–2D coupled model is 2.0. Thus, it is clear that the 1D–2D coupled model is more efficient in shallow water simulations.

5.4. Curved channel flow simulation

A channel with a 180° constant curvature bend is schematically shown in Fig. 13 for the 2D and 1D–2D coupled models. The channel has a width of 0.8 m and was originally designed by Rozovskii (1961). Table 4 illustrates the locations of the inflow/outflow boundaries in the 1D domain. This curved channel consists of an inner radius with a curvature of 0.4 m and an outer radius with a curvature of 1.2 m. Manning's roughness coefficient is adopted as 0.011 s/m$^{1/3}$ in this study. The water discharge and water depth are set to 0.0123 m^3/s and 0.058 m at the inflow and outflow boundaries, respectively. The initial particle spacing is equal to 0.02 m in both the 1D and 2D models, and the maximum time step is 0.015 s.

Fig. 14 gives the simulated contours of water depths and the profiles of water velocity vectors for the two SPH-SWE models. In Fig. 14(c) and (d), the water velocity along the inner wall increases as flow passes through the front part of the bend. Then, the water velocity decreases as flow exits the bend. Along the outer wall, flow deacceleration occurs within the front part of the bend, and flow acceleration then occurs as the flow exits the bend. Hence, the water depth along the inner wall is lower than that along the outer wall, as schematically illustrated in Fig. 14(a) and (b).

The magnitudes of water velocities along the radial axis at the angles of 0°, 35°, 65°, 100°, 143° and 186° are compared with the data collected by Rozovskii (1961) and the FDM-based simulation results of Lien et al. (1999), as shown in Fig. 15. The simulated water velocity magnitudes exhibit good agreement with the measured data, except the results predicted in the vicinity of the inner wall. Due to the use of a non-slip boundary condition, the magnitudes of water velocities in the vicinity of the inner wall computed by the two SPH-SWE models are lower than the measured values. Fig. 16 presents the simulated water discharge for the two SPH-SWE models. The degree of satisfaction of the mass conservation constraint in the 1D–2D coupled model can be determined using Eq. (28). Specifically, $L_2(Q)$ in the 1D domain is 6.94E−03, and $L_2(Q)$ in the 2D domain is 1.75E−03. As listed in Table 5, the convergence rates based on the water discharge in the 1D and 2D domains are 1.07 and 1.15, respectively. Thus, the two SPH-SWE models are both applicable to simulations of curved channel flows. However, as shown in Table 3, the 1D–2D coupled model yields a higher efficiency than the 2D model.

6. Concluding remarks

In this study, the proposed 1D and 2D coupled SPH-SWE model was validated based on three subcritical flows in converging, diverging and curved channels. The simulation results compare well with measured data and mesh-based numerical results. Model convergence based on water discharge was investigated to verify that the proposed SPH model yields first-order convergent solutions in 1D and 2D domains. Additionally, we confirmed that the proposed model produces results that are quantitively comparable to those based on 2D SPH-SWEs, but the results of the couple model require a much smaller CPU time. Furthermore, incorporating the continuity equation and an externally added density diffusion term into the model yielded more accurate and efficient predictions of water depth than those based on the SPH summation operator. The convergence rate of the continuity approach can reach approximately unity. Conversely, the water depth errors close to the wall boundaries result in lower convergence rates for the summation approach. In summary, the proposed 1D–2D coupled SPH-SWE model is a potential alternative for numerical simulations of open channel flows bounded by irregularly shaped walls.

Acknowledgments

We thank the Ministry of Science and Technology of Taiwan (MOST 106-2917-I-564-045) for financially supporting this study.

References

Altomare, C., Domínguez, J.M., Crespo, A.J.C., Suzuki, T., Caceres, I., Gómez-Gesteira, M., 2015. Hybridization of the Wave Propagation Model SWASH and the Meshfree Particle Method SPH for real coastal applications. Coast. Eng. J. 57 (4), 1550024.
Arico, C., Filianoti, P., Sinagra, M., Tucciarelli, T., 2016. The FLO diffusive 1D-2D model for simulation of river flooding. Water 8 (5), 200.
Ata, R., Soulaimani, A., 2005. A stabilized SPH method for inviscid shallow water flows. Int. J. Numer. Methods Fluids 47 (2), 139–159.
Biglari, B., Sturm, T.W., 1998. Numerical modeling of flow around bridge abutments in compound channel. J. Hydraul. Eng. 124 (2), 156–164.
Blade, E., Gomez-Valentin, M., Dolz, J., Aragon-Hernandez, J.L., Corestein, G., Sanchez-Juny, M., 2012. Integration of 1D and 2D finite volume schemes for computations of water flow in natural channels. Adv. Water Resour 42, 17–29.
Bonet, J., Lok, T.-S.L., 1999. Variational and momentum preservation aspects of Smooth Particle Hydrodynamic formulations. Comput. Methods Appl. Mech. Eng. 180, 97–115.
Bouscasse, B., Colagrossi, A., Marrone, S., Antuono, M., 2013. Nonlinear water wave interaction with floating bodies in SPH. J. Fluid Struct. 42, 112–129.
Burguete, J., Garcia-Navarro, P., Murillo, J., 2008. Friction term discretization and limitation to preserve stability and conservation in the 1D shallow-water model: application to unsteady irrigation and river flow. Int. J. Numer. Methods Fluids 58 (4), 403–425.
Chang, K.H., Chang, T.J., Chiang, Y.M., 2016a. A novel SPH-SWEs approach for modeling subcritical and supercritical flows at open channel junctions. J. Hydro-Environ. Res. 13, 76–88.
Chang, K.H., Chang, T.J., Sheu, T.W.H., 2017. Development of an upwinding kernel in SPH-SWEs model for 1D trans-critical open channel flows. J. Hydro-Environ. Res. 15, 13–26.
Chang, T.J., Chang, K.H., 2013. SPH modeling of one-dimensional nonrectangular and nonprismatic channel flows with open boundaries. J. Hydraul. Eng. 139 (11), 1142–1149.
Chang, T.J., Chang, Y.S., Chang, K.H., 2016b. Modeling rainfall-runoff processes using smoothed particle hydrodynamics with mass-varied particles. J. Hydrol. 543 (B), 749–758.
Chang, T.J., Kao, H.M., Chang, K.H., Hsu, M.H., 2011. Numerical simulation of shallow-water dam break flows in open channels using smoothed particle hydrodynamics. J. Hydrol. 408 (1-2), 78–90.
Chaudhry, M.H., 2008. Open-Channel Flow. Prentice-Hall, New Jersey.
Chen, R., Shao, S., Liu, X., Zhou, X., 2015. Applications of shallow water SPH model in mountainous rivers. J. Appl. Fluid Mech. 8 (4), 863–870.
Choi, G.W., Molinas, A., 1993. Simultaneous solution algorithm for channel network modeling. Water Resour. Res 29 (2), 321–328.

Colagrossi, A., Landrini, M., 2003. Numerical simulation of interfacial flows by smoothed particle hydrodynamics. J. Comput. Phys. 191 (2), 448–475.
Federico, I., Marrone, S., Colagrossi, A., Aristodemo, F., Antuono, M., 2012. Simulating 2D open-channel flow through an SPH model. Eur. J. Mech. B-Fluid 34, 35–46.
Fernandez-Nieto, E.D., Marin, J., Monnier, J., 2010. Coupling superposed 1D and 2D shallow-water models: source terms in finite volume schemes. Comput. Fluids 39 (6), 1070–1082.
Gingold, R.A., Monaghan, J.J., 1977. Smoothed particle hydrodynamics - theory and application to non-spherical stars. Mon. Not. R. Astron. Soc 181 (2), 375–389.
Gong, K., Shao, S.D., Liu, H., Wang, B.L., Tan, S.K., 2016. Two-phase SPH simulation of fluid-structure interactions. J. Fluid Struct. 65, 155–179.
Gu, S., Zheng, X., Ren, L., Xie, H., Huang, Y., Wei, J., Shao, S.D., 2017. SWE-SPHysics simulation of Dam Break Flows at South-Gate Gorges Reservoir. water 9 (6), 387–406.
Hernquist, L., Katz, N., 1989. TREESPH: a unification of SPH with the hierarchical tree method. Astrophys. J. Suppl. Ser. 70 (2), 419–446.
Hsu, M.H., Fu, J.C., Liu, W.C., 2003. Flood routing with real-time stage correction method for flash flood forecasting in the Tanshui River. Taiwan, J. Hydrol 283 (1-4), 267–280.
Kao, H.M., Chang, T.J., 2012. Numerical modeling of dambreak-induced flood and inundation using smoothed particle hydrodynamics. J. Hydrol. 448, 232–244.
Lien, H.C., Hsieh, T.Y., Yang, J.C., Yeh, K.C., 1999. Bend-flow simulation using 2D depth-averaged model. J. Hydraul. Eng. 125 (10), 1097–1108.
Lucy, L.B., 1977. Numerical approach to testing of fission hypothesis. Astron. J. 82 (12), 1013–1024.
Marin, J., Monnier, J., 2009. Superposition of local zoom models and simultaneous calibration for 1D-2D shallow water flows. Math. Comput. Simulat 80 (3), 547–560.
Molteni, D., Colagrossi, A., 2009. A simple procedure to improve the pressure evaluation in hydrodynamic context using the SPH. Comput. Phys. Commun. 180 (6), 861–872.
Monaghan, J.J., 1992. Smoothed particle hydrodynamics. Annu. Rev. Astron. Astr. 30, 543–574.
Monaghan, J.J., 1994. Simulating free-surface flows with SPH. J. Comput. Phys 110 (2), 399–406.
Morales-Hernandez, M., Garcia-Navarro, P., Burguete, J., Brufau, P., 2013. A conservative strategy to couple 1D and 2D models for shallow water flow simulation. Comput. Fluids 81, 26–44.
Morales-Hernandez, M., Petaccia, G., Brufau, P., Garcia-Navarro, P., 2016. Conservative 1D-2D coupled numerical strategies applied to river flooding: the Tiber (Rome). Appl. Math. Model 40 (3), 2087–2105.
Nadaoka, K., Yagi, H., 1998. Shallow-water turbulence modeling and horizontal large-eddy computation of river flow. J. Hydraul. Eng. 124 (5), 493–500.
Narayanaswamy, M., Crespo, A.J.C., Gomez-Gesteira, M., Dalrymple, R.A., 2010. SPHysics-FUNWAVE hybrid model for coastal wave propagation. J. Hydraul. Res. 48 (SI), 85–93.
Randles, P.W., Libersky, L.D., 1996. Smoothed particle hydrodynamics: some recent improvements and applications. Comput. Methods Appl. Mech. and Eng. 139 (1-4), 375–408.
Rodriguez-Paz, M., Bonet, J., 2005. A corrected smooth particle hydrodynamics formulation of the shallow-water equations. Comput. Struct. 83 (17-18), 1396–1410.
Rozovskii, I.L., 1961. Flow of Water in Bends of Open Channels. The Israel Program for Scientific Translations, Jerusalem.
Sanders, B.F., Green, C.L., Chu, A.K., Grant, S.B., 2001. Case study: modeling tidal transport of urban runoff in channels using the finite-volume method. J. Hydraul. Eng. 127 (10), 795–804.
Sen, D.J., Garg, N.K., 1998. Efficient solution technique for dendritic channel networks using FEM. J. Hydraul. Eng. 124 (8), 831–839.
Shao, S.D., Gotoh, H., 2004. Simulating coupled motion of progressive wave and floating curtain wall by SPH-LES model. Coast. Eng. J. 46 (2), 171–202.
Shao, S.D., Lo, E.Y.M., 2003. Incompressible SPH method for simulating Newtonian and non-Newtonian flows with a free surface. Adv. Water Resour. 26, 787–800.
Shettar, A.S., Murthy, K.K., 1996. A numerical study of division of flow in open channels. J. Hydraul. Res. 34 (5), 651–675.
Song, C.G., Seo, I.W., Do Kim, Y., 2012. Analysis of secondary current effect in the modeling of shallow flow in open channels. Adv. Water. Resour. 41, 29–48.
Unami, K., Kawachi, T., Babar, M.M., Itagaki, H., 1999. Two-dimensional numerical model of spillway flow. J. Hydraul. Eng. 125 (4), 369–375.
Vacondio, R., Rogers, B.D., Stansby, P.K., 2012b. Smoothed particle hydrodynamics: approximate zero-consistent 2-D boundary conditions and still shallow-water tests. Int. J. Numer. Methods Fluids 69 (1), 226–253.
Vacondio, R., Rogers, B.D., Stansby, P.K., Mignosa, P., 2012a. SPH modeling of shallow flow with open boundaries for practical flood simulation. J. Hydraul. Eng. 128 (6), 530–541.
Violeau, D., 2012. Fluid Mechanics and the SPH Method: Theory and Applications. Oxford University Press, United Kingdom.
Wang, Z., Shen, H.T., 1999. Lagrangian simulation of one-dimensional dam-break flow. J. Hydraul. Eng. 125 (11), 1217–1220.
Weber, L.J., Schumate, E.D., Mawer, N., 2001. Experiments on flow at a 90 degrees open-channel junction. J. Hydraul. Eng. 127 (5), 340–350.
Xia, X., Liang, Q., Pastor, M., Zou, W., Zhuang, Y.F., 2013. Balancing the source terms in a SPH model for solving the shallow water equations. Adv. Water. Resour. 59, 25–38.
Ying, X.Y., Khan, A.A., Wang, S.S.Y., 2004. Upwind conservative scheme for the saint Venant equations. J. Hydraul. Eng. 130 (10), 977–987.